Non-Oxidative Mechanism in Oxygen-Based Magneto-Ionics

Tanvi Bhatnagar-Schöffmann, Patrick Schöffmann, Andrea Resta, Alessio Lamperti, Guillaume Bernard, András Kovács, Ludovic Largeau, Alan Durnez, Abdelmounaim Harouri, Xavier Lafosse, Djoudi Ourdani, Maria-Andromachi Syskaki, Yves Roussigné, Shimpei Ono, Rafal E. Dunin-Borkowski, Jürgen Langer, Dafiné Ravelosona, Mohamed Belmeguenai, Aurelie Solignac, and Liza Herrera Diez*

The Ta/CoFeB/Pt/MgO/HfO$_2$ system is investigated, whose magnetic anisotropy can be controlled through magneto-ionic gating, using both ionic liquid and solid state gating, via a non-oxidative mechanism combining reversible and irreversible gating effects. Analysis of X-ray absorption spectroscopy at the Co and Fe edges reveals no indications of oxidation after gating, while a reversible change at the oxygen K edge suggests the involvement of oxygen species in the magneto-ionic process. In addition, X-ray diffraction measurements reveal that gating can irreversibly increase the crystalline volume of MgO, through an increase in the MgO/Mg(OH)$_2$ ratio. This is in line with measurements in solid state devices showing that in a series of 150 gating cycles a reversible effect combines with a progressive increase in the strength of the perpendicular magnetic anisotropy contribution that saturates after extensive cycling. Consequently, the observed gate-induced changes in magnetic anisotropy can be attributed to the combined effects of Mg(OH)$_2$ dehydration into MgO (irreversible) and most likely a gentle reordering of oxygen species at the CoFeB interface (reversible) leading to a non-oxidative magneto-ionic mechanism. This study provides valuable insights into the underlying mechanisms governing the complex magneto-ionic phenomena, including the coexistence of both reversible and irreversible effects, and a pathway to voltage-control of crystalline order in spintronics materials.

1. Introduction

Magneto-ionics, the control of magnetic properties by gate-voltage-induced ionic motion, constitutes an attractive path toward low-power spintronics applications, such as magnetic memories and logic devices. In this context, oxygen-based magneto-ionics has emerged as a promising avenue for the non-volatile manipulation and control of magnetic properties in ferromagnet/oxide systems.[1,2] The prevailing understanding in the field is that the observed non-volatile voltage-induced changes in magnetic anisotropy, typically between in-plane anisotropy (IPA) and perpendicular anisotropy (PMA), are primarily due to a gate-voltage-controlled oxidation/reduction at the metal/oxide interface. Several studies have shown evidence of gate-voltage-induced oxidation in a number of systems, in particular where the magnetic material is interfaced with HfO$_2$,[3,4] which is accompanied by a loss of magnetic moment. Therefore, when oxygen magneto-ionics is at play, an oxidation/reduction mechanism is commonly assumed.

T. Bhatnagar-Schöffmann, G. Bernard, L. Largeau, A. Durnez, A. Harouri, X. Lafosse, D. Ravelosona, L. Herrera Diez
Centre de Nanosciences et de Nanotechnologies
CNRS, Université Paris-Saclay
91120 Palaiseau, France
E-mail: liza.herrera-diez@c2n.upsaclay.fr
P. Schöffmann, A. Resta
Synchrotron SOLEIL
L'Orme des Merisiers, 91190 Saint-Aubin, France

A. Lamperti
IMM-CNR
Unit of Agrate Brianza
Via C. Olivetti 2, 20864 Agrate Brianza (MB), Italy
A. Kovács, R. E. Dunin-Borkowski
Ernst Ruska-Centre for Microscopy and Spectroscopy with Electrons
Peter Grünberg Institute, Forschungszentrum Jülich GmbH
52425 Jülich, Germany
D. Ourdani, Y. Roussigné, M. Belmeguenai
Laboratoire des Sciences des Procédés et des Matériaux,
CNRS-UPR 3407
Université Sorbonne Paris Nord
93430 Villetaneuse, France
M.-A. Syskaki, J. Langer
Singulus Technology AG
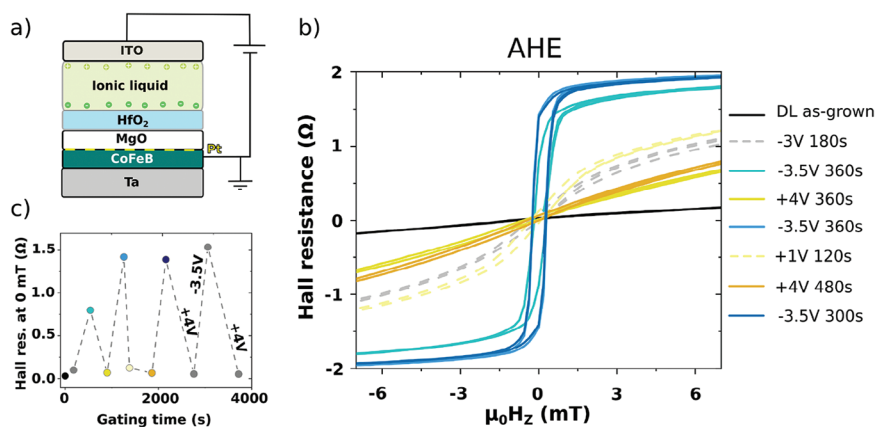Hanauer Landstrasse 103, 63796 Kahl am Main, Germany

Figure 1. a) Illustration of the structure of the magneto-ionic device containing an ionic liquid gate. b) Anomalous Hall effect (AHE) hysteresis loops as a function of $\mu_0 H_z$ for the as-grown DL layer and after exposure to a sequence of gate voltages. c) Hall resistance at 0 mT for the voltage cycles shown in (b) (same colour code) and additional points measured for a +4 V/−3.5 V/+4 V gate voltage application sequence.

In this study, we demonstrate that oxygen magneto-ionics can also operate without inducing oxidation of the magnetic atoms. We investigate the Ta/CoFeB/Pt(dusting layer)/MgO/HfO$_2$ system, where the Pt dusting layer (DL) between CoFeB and MgO largely suppresses the oxidation naturally happening at this interface during growth. The presence of the dusting layer, in consequence, weakens the magnetic anisotropy that builds at the CoFeB/MgO interface, so that a spin-reorientation transition can be induced using gate voltages[5] in both ionic liquid gating and solid state gating devices. The Pt dusting layer also favors the crystallization of MgO during growth. Ionic-liquid gating has been employed to show that no signs of oxidation are observed across the gate-induced spin-reorientation transition in this system, while changes in structural properties compatible with a gate-induced conversion of Mg(OH)$_2$ into MgO are observed. We therefore propose an alternative mechanism for oxygen-based magneto-ionics, that does not involve the oxidation of the magnetic atoms at the interface with the oxide, but rather a combined effect of a reversible non-oxidative interaction between oxygen and Fe/Co and an irreversible voltage-induced change in the crystalline and chemical structure within the MgO layer.

2. Results and Discussion

The magnetic stack used in this study, Ta(5 nm)/Co$_{40}$Fe$_{40}$B$_{20}$-(1 nm)/Pt(0.09 nm)/MgO(2 nm)/HfO$_2$(3 nm), is grown by magnetron sputtering, the magneto-ionic device containing an ionic liquid gate is depicted in **Figure 1a** (see the Experimental Section). It was shown in a previous study that in this material the

MgO layer is textured before and after ionic-liquid gating.[5] The presence of Pt has been found to be crucial to the appearance of crystalline order in the MgO layer, as layers without a Pt dusting layer show an amorphous structure in transmission electron microscopy measurements (TEM, see Supporting Information).

As previously reported,[5] a clear spin reorientation transition from a dominant IPA to a dominant PMA is evidenced after applying negative gate voltages to the top ITO electrode of the gate, and the PMA state that is obtained can be subsequently weakened by applying positive gate voltages. This behavior is shown in Figure 1b through anomalous Hall effect (AHE) measurements conducted under a magnetic field perpendicular to the sample plane ($\mu_0 H_z$). Starting from an as-grown DL sample (containing a Pt dusting layer) several subsequent cycles of gate voltage applications of negative and positive gate voltages reversibly drive a spin-reorientation transition. A first application of −3 V for 180s shows a relatively small increase in the PMA component, while a subsequent application of −3.5 V for 360 s can stabilize a dominant PMA component. A subsequent application of +4 V for 360 s reverts the system to a state dominated by IPA. Several subsequent voltage applications are presented in Figure 1b, which show the reversibility of the system. It is also shown that using lower gate voltages than −3.5 V/+4 V leads to the stabilization of non-volatile intermediate states between the IPA and PMA dominated states, as seen for −3 V and +1 V, shown in Figure 1b by dotted lines. Figure 1c shows the Hall resistance at remanence (0 mT) for all the measurements presented in (b) as well as for further voltage applications with the sequence +4 V/−3.5 V/+4 V. Additional magnetometry measurements can be found in the Supporting Information.

In order to gain insight into the effects of the magneto-ionic gating on the oxidation state of Fe and Co atoms, XAS measurements were conducted. **Figure 2a** and **2c** display the XAS spectra of Fe and Co for the DL as-grown sample, both before and after applying a gate voltage of −3.5 V for 360 s, followed by a subsequent application of +4 V for 360 s. The spectra are normalized to the peak intensity of the L$_3$ K-edges. Although significant changes in the magnetic anisotropy are observed under these gating conditions, as shown in Figure 1, no changes in the oxidation state (see zoom-in of the L$_3$ edges in the insets) of neither

S. Ono
Central Research Institute of Electric Power Industry
Yokosuka, Kanagawa 240-0196, Japan

D. Ravelosona
Spin-Ion technologies, C2N
10 Boulevard Thomas Gobert, 91120 Palaiseau, France

A. Solignac
SPEC, CEA, CNRS, Université Paris-Saclay, CEA Saclay
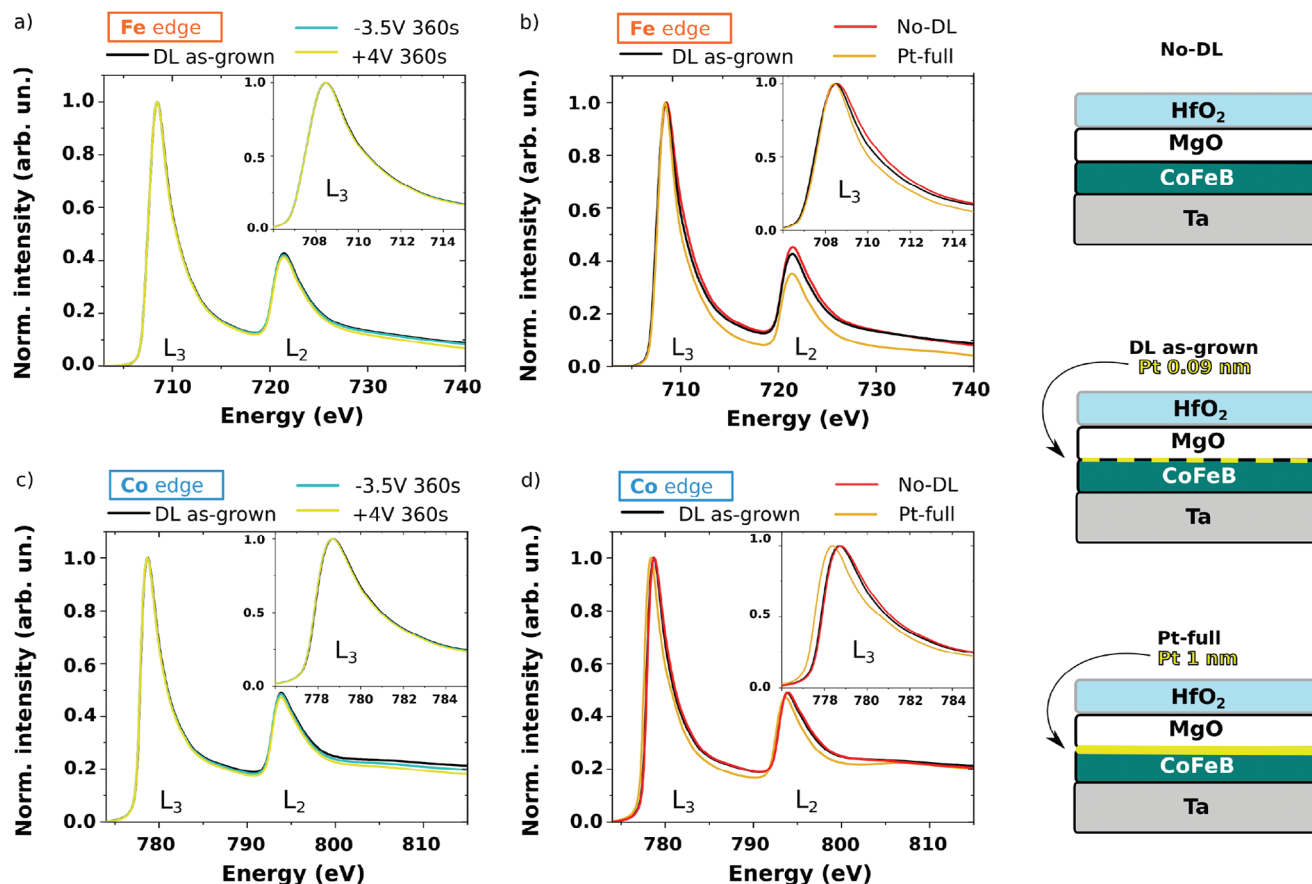91191 Gif-sur-Yvette Cedex, France

Figure 2. Normalized XAS spectra of the (a) Fe and (b) Co K-edges measured for the DL as-grown sample before and after a gate voltage application of −3.5 V for 360 s, and a subsequent application of +4 V for 360 s. a) Fe and b) Co edges were also measured for samples No-DL and Pt-full. All insets show a zoomed-in view of the L_3 edge. The cartoons on the right hand side depict the structures of samples DL, No-DL and Pt-full.

Fe nor Co are observed. In order to verify that interface oxidation effects can be detected in these experiments, samples without a Pt dusting layer (No-DL) and with a full 1 nm Pt layer (Pt-full) between the CoFeB and MgO layers were investigated as references for CoFeB layers containing a higher or lower degree of oxidation with respect to the DL sample, respectively. Significant changes are observed in the normalized XAS Fe and Co edges of samples No-DL and Pt-full, as presented in Figure 2b,d, respectively. The zoomed-in view of the L_3 edge of Fe shows a visible increase in the signal on the higher energy side of the peak for the No-DL sample and a decrease in the signal for the Pt-full sample with respect to the DL as-grown sample. This increase in the signal in the No-DL sample can be attributed to the presence of higher oxidation states in Fe[6–8] whereas, the decrease in the signal for the Pt-full sample may arise from the opposite effect, which is a reduced interaction between Fe and O due to the presence of the 1 nm thick Pt layer separating CoFeB from MgO. The Co edge shows a similar behavior between the DL and No-DL samples, however, the spectrum of the Pt-full sample shows a relatively large shift of more than 0.3 eV toward lower energies compared to both the DL and No-DL samples, which was not observed in the Fe edge. This can also be in part attributed to a reduced interaction with oxygen, however, it may also be linked to a strong interaction between Pt and Co that could pro-

vide Co atoms with an increased stability against oxidation.[6,9] This shift of the absorption edge toward lower energies has been already observed in very thin layers of Co grown on Pt substrates, which may be subjected to a strong interaction between Co and Pt.[6]

In the No-DL sample, the observed signs of oxidation are accompanied by a reduction of the magnetic moment per unit area and a corresponding reduction in the CoFeB layer thickness, determined by X-ray reflectivity measurements (see Supporting Information), going from 0.99 nm for the DL sample to 0.64 nm for the No-DL sample. Most importantly, the No-DL sample, unlike the DL sample, shows PMA in the as-grown state. These observations can be directly correlated with the well-known oxidative mechanism giving rise to PMA at the CoFeB/MgO interface. In contrast, the DL sample after gating does not only show PMA without signs of oxidation but also shows no significant changes in the magnetic moment, and a relatively small thickness variation going from 0.99 nm in the as-grown state to 0.866 nm after gating under a negative gate voltage, which can be attributed to a gate induced reordering of atoms at the CoFeB(Pt)/MgO interface. The observation of these two mechanisms in two similar samples shows that both mechanisms could potentially coexist, however, the non-oxidative effects could be shadowed in the presence of an oxidative mechanism. This is confirmed by the
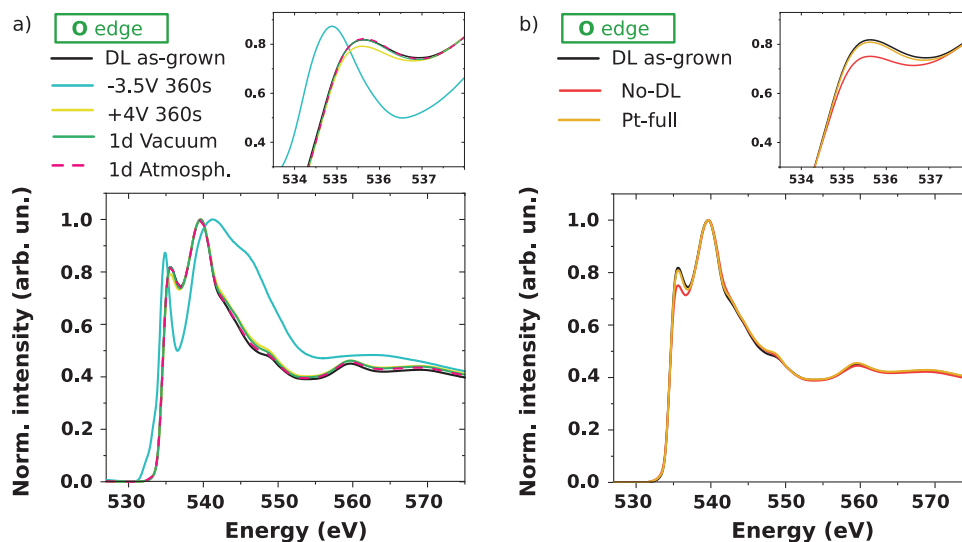
Figure 3. Normalized XAS spectra of the oxygen K-edge measured for (a) the DL as-grown sample before and after a gate voltage application of −3.5 V for 360 s, subsequent application of +4 V for 360 s, subsequent one day evolution in vacuum, and subsequent one day evolution exposed to the atmosphere. b) Oxygen K-edge in the DL as-grown, No-DL and Pt-full samples. All insets show a zoomed-in view of the spectra for energies between 534–538 eV.

estimation of the effective magnetic anisotropy (K_{eff}) of the No-DL sample and the DL sample after exposure to a negative voltage (see Supporting Information) which are 3.2×10^{-5} Jm^{-3} and 1.3×10^{-4} Jm^{-3}, respectively. Intefacial oxidation gives rise to a perpendicular K_{eff} that is more than one order of magnitude larger than that of the non-oxidative mechanism presented here, which confirms the potentiality for larger amplitudes of the magneto-ionic effects on PMA through an oxidative mechanism.

The oxygen K-edge signal was also analyzed, however, unlike that of Co and Fe edges, it contains a complex convolution of different contributions coming from multiple layers in the stack such as Fe and Co oxides,[10,11] MgO and HfO$_2$ and it may also contain a contribution from H$_2$O and products of its dissociation such as OH- groups,[7,12] which can be expected when magneto-ionic gating is involved.[13] Peaks at relatively high energies starting from about 534 eV can be attributed to O-Hf hybridization[14,15] and to O-Mg hybridization, as well as to changes in the crystalline structure of MgO during annealing.[7,16] Pre-edge structures can also be observed between 528 eV and 534 eV and can be typically linked to the hybridization between O and Fe orbitals.[7,16,17] Pre-edge features have also been detected in MgO thin films and substrates, which was correlated to the crystalline structure.[18] HfO$_2$ films can also present pre-edge features related to the presence of oxygen vacancies.[19] This makes the analysis of the Oxygen K-edge structure in this system a very complex task. However, a qualitative comparison between the spectra from the DL gated samples and the No-DL and Pt-full samples can bring additional information to the analysis.

The normalized oxygen K-edge XAS spectra of the DL sample as-grown, after voltage application, and after time evolution, are shown in **Figure 3**a, while the spectra for samples DL as-grown, No-DL and Pt-full are shown in Figure 3b. The most prominent feature seen in the sample series DL, No-DL and Pt-full has peaks at approximately 535 and 540 eV as shown in Figure 3b. A fitting

of the spectrum of the as-grown DL sample using reference data of Oxygen K-edge signals of MgO[18] and HfO$_2$[20] provides a good qualitative agreement, suggesting that the spectra of the DL, No-DL and Pt-full samples are mainly dominated by these two contributions (see Supporting Information). The DL and Pt-full samples show a very similar profile across the whole energy range, while the No-DL sample shows a decrease in intensity of the peak centerd at $\approx$ 535.5 eV. Similar features in this energy range have been attributed to O-Mg interactions,[21] while in Fe/MgO, an increase in intensity in the energy range between 535 and 540 eV has been related to an increase in crystallinity of the MgO layer after annealing.[7] Therefore, in the present case, the reduced intensity in the No-DL sample may be related not only to the effects of oxidation at the CoFeB/MgO interface but also to a lower degree of crystalline order in the MgO layer, due to the absence of the Pt dusting layer.

Applying a gate voltage of −3.5 V for 360 s to the DL sample induces drastic changes in the Oxygen K-edge profile as seen in Figure 3a. The double peak feature seen in the as-grown DL sample shows a larger separation between the peaks, and new features appear at energies above 540 eV. Pre-edge features are also observed after gating, which can typically be assigned to oxidation of Fe and Co,[7] but are absent in the No-DL sample, and are also not accompanied by oxidation features in the Fe and Co edges. These large differences in the oxygen k-edge signals obtained for the gated DL sample under negative voltages and the No-DL sample behavior can therefore not be directly correlated to the surface oxidation present in the No-DL sample. Figure 3a shows that a positive gate voltage induces the recovery of the signal profile of the DL as-grown sample, which corresponds well with the observed reversibility of the gating effects on the magnetic properties presented in Figure 1. A reduction of the intensity of the signal at the peak center located at $\approx$ 535.5 eV is observed after gating with positive voltage, however, unlike the signal of the No-DL sample, this difference is significantly smaller

2300955 (4 of 10)

ADVANCED
SCIENCE NEWS

www.advancedsciencenews.com

ADVANCED
MATERIALS
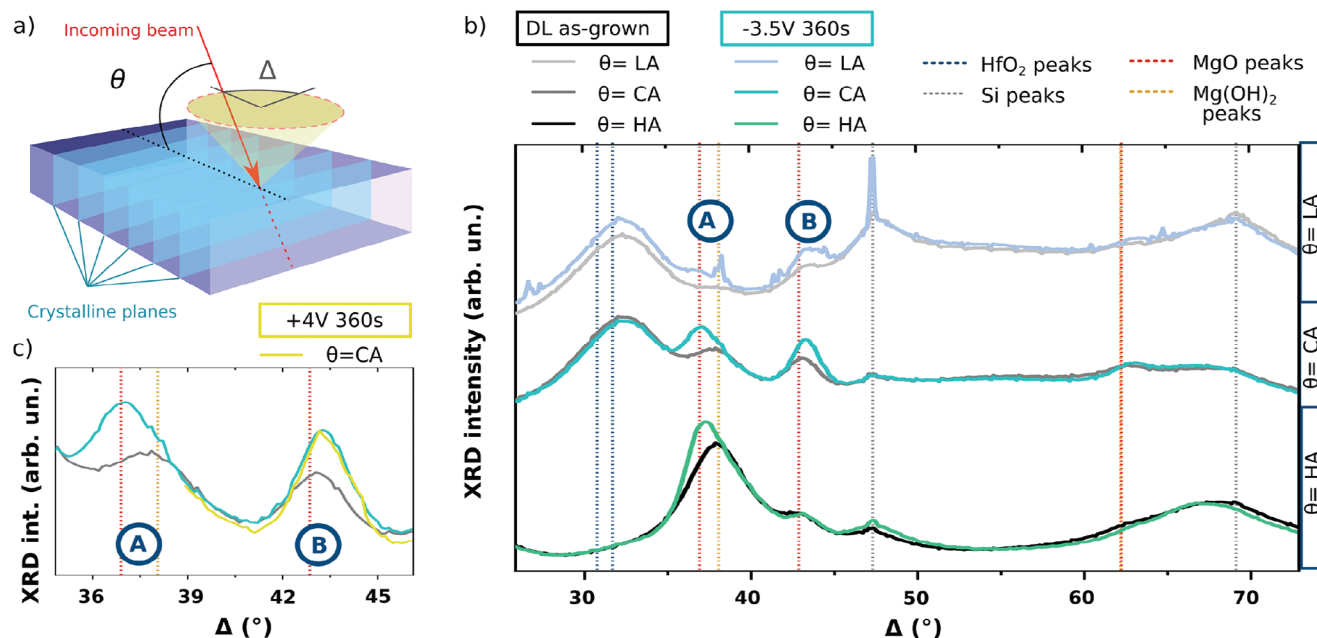**INTERFACES**
Open Access

www.advmatinterfaces.de

Figure 4. a) X-ray diffraction measurement geometry and b) in-plane X-ray diffraction maps as a function of Δ. The maps were recorded in DL as-grown and gated samples at different grazing incidence angles θ: 0.4577°, lower than the critical angle of total reflection (LA), 0.7780°, at the critical angle (CA), and 1.3730°, higher than the critical angle (HA). The relevant bulk indexed peaks of MgO, MgO(OH)$_2$, HfO$_2$ and Si are indicated by vertical lines. c) Zoom-in of peaks A and B.

and it is lost after letting the sample evolve for one day in vacuum. In addition, this feature is seen after the application of a positive voltage to the top electrode, which is highly unfavorable to oxidation at the surface of the CoFeB and it is also not accompanied by changes in the Fe and Co edges, unlike the case of the No-DL sample. The time evolution of the oxygen K-edge after positive voltage application can be correlated to the reported time evolution of the IPA state achieved after the application of positive gate voltages. The IPA state achieved after the application of positive gate voltages evolves toward a state with increased PMA over the following days.[5] In the present case, as the gate-induced changes in magnetic properties occur via a non-oxidative process, a relatively weak interaction between mobile oxygen species and the magnetic atoms is expected, which could naturally lead to the time evolution effects observed. The analysis of the Oxygen K-edge reveals that the reversible gating effects seen in the magnetic anisotropy are well reflected in the chemical environment of the oxygen atoms in the layer, despite the absence of any features in the Co and Fe edges, confirming a mechanism that is oxygen-based but non-oxidative in nature.

Despite the great complexity of the oxygen K-edge in this system and of the changes observed after gating under negative voltages, strong similarities are seen between the signal after negative-voltage gating and the reported signature of uncoordinated OH- groups in water.[7,12] In addition, Pt based materials are extensively used as very efficient catalysts mostly for hydrogen gas production through water splitting.[22] Not only Pt-rich surfaces, but even surfaces with dispersed single Pt atoms have been reported to show a very high catalytic performance,[23,24] including systems where the Pt is supported by Fe oxide nanocrystallites.[25] Therefore, the presence of a dusting layer of Pt at the interface between CoFeB and MgO, could

have an impact on the formation and splitting of water molecules at the interface, and could be at the origin of the large differences in the oxygen K-edge signal after negative-voltage gating. The presence of water and water-splitting products at the MgO interface could facilitate a potential gate-driven hydration of the MgO layer to form Mg(OH)$_2$, and vice-versa. Hydration (thermal dehydration) of MgO (Mg(OH)$_2$) is well documented in the literature[26–31] and in particular, the dehydration of Mg(OH)$_2$ into MgO has been discussed in the context of the development of strategies to improve interface quality in CoFeB/MgO based stacks and magnetic tunnel junctions.[7,32–34]

A potential hydration/dehydration process of the MgO/Mg(OH)$_2$ can have a large impact on the crystalline order of the system, as MgO hydration can lead to the formation of Mg(OH)$_2$ with brucite-like crystalline structure.[7,28,31] Therefore, the evaluation of a potential gate-induced MgO hydration/dehydration mechanism requires an investigation of the effects of gating on the crystalline structure of the MgO layer. To this end, in-plane X-ray diffraction maps were conducted at different grazing incidence angles θ: (I) 0.4577°, lower than the critical angle of total reflection (LA), (II) 0.7780°, at the critical angle (CA), and (III) 1.3730°, higher than the critical angle (HA). LA has a very low penetration depth, thus only the top part of the film is visible, then for CA and HA, the beam probes progressively deeper regions of the sample. **Figure 4a** shows the measurement geometry, where θ represents the incidence angle with respect to the surface of the sample, while Δ represents the angles at which the sample rotates with respect to the incident beam, in order to probe all in-plane directions. As shown in Figure 4b the integration curves for in-plane diffraction maps at LA do not present any significant changes before and after gating, however, it is interesting to analyze the broad

feature centerd around $\theta = 32°$. This feature is in the vicinity of the indexed peak of HfO_2 (111) in the monoclinic phase ($\Delta = 31.67°$). It has been seen in TEM measurements that in both as-grown DL and gated samples the HfO_2 layer does not show any crystalline structure.[5] Therefore, any HfO_2-related diffraction signal is expected to be broad and to come from relatively small crystallites. This broad feature is still visible, with minor differences, in the integration curves taken at CA. However, it is strongly suppressed in the HA curves, which probes deeper regions of the sample, supporting the idea of it being related to the HfO_2 layer. In the CA curves, a clear gating effect is observed in the features labeled A and B. Peak A, in the DL as-grown film has a maximum that aligns well with the indexed peak of $Mg(OH)_2$ (011) (Δ 38.05°), it also has a higher intensity on the low Δ side, which can be attributed to a convolution with a peak appearing near the position of the MgO (111) peak, located at $\Delta = 36.89°$. After negative gate voltage application, the maximum of the peak shifts towards the position of the MgO (111) peak, accompanied by an increase in intensity. In the case of peak B, the maximum is located near the MgO (200) peak ($\Delta = 42.85°$) where a significant increase of intensity is observed after gating. In the HA curves, the change of ratios and intensities seen near the positions of the $Mg(OH)_2$ (011) and MgO (111) peaks in the CA curves are reproduced. In all integration curves, smaller features are also seen near the $Mg(OH)_2$ (111) and MgO (220), at 62.17° and 62.23°, respectively. Finally, due to the strong beam flux, Si substrate peaks are visible in all three maps, in particular peaks of Si (220) ($\Delta = 47.3°$) and Si (400) ($\Delta = 69.14°$).

As mentioned earlier, the peaks associated to HfO_2 are visible for LA and CA, and are highly suppressed for HA, due to the increasing probing depth when going from LA to HA. In agreement with this notion, the peaks associated to $MgO/Mg(OH)_2$, are more visible for CA and HA than for LA. Most importantly, these maps allow for the observation of gate-sensitive peaks associated to both MgO and $Mg(OH)_2$. The gate-driven changes observed in peak A (see zoomed-in scale in Figure 4c) indicate a gate-driven modification of the $MgO/Mg(OH)_2$ ratio in the stack. In addition, the relative increase in intensity of peak B, associated to MgO, indicates an overall increase in the MgO crystallinity in the layer after the application of a negative gate voltage (-3.5 V for 360 s). In this context, a scenario where the initially hydrated MgO layer, containing $Mg(OH)_2$, can be dehydrated by the action of a negative gate voltage can be proposed as an ionic mechanism that can significantly contribute to the changes observed in magnetic anisotropy after the application of a negative gate voltage. Figure 4c also shows a local CA map measured around peak B in a sample where a positive gate voltage (+4 V for 360 s) was applied subsequently after an initial negative voltage application (-3.5 V for 360 s), which does not induce any significant changes. Peak A is not presented due to the presence of an interference signal, unrelated to the sample structure, occurring within the same angle range (see Supporting Information). This strongly suggests the irreversible increase in the crystalline volume of the MgO layer at the expense of a gate-induced dehydration of $Mg(OH)_2$.

The thermal dehydration mechanism of $Mg(OH)_2$, where MgO and H_2O are produced, as well as the interaction of MgO with hydroxyl groups has been widely studied both experimentally and theoretically.[28,31,35–40] In particular, the different possi-ble binding sites of hydroxyl groups and their role in the dehydration process are subject of intense investigation. Several studies demonstrate that $Mg(OH)_2$ grows in a layered structure on top of MgO, and propose the presence of hydroxyl groups with a higher or lower degree of coordination,[28,37,39] including hydroxyl groups located between layers. These hydroxyl groups are coordinated by the neighboring Mg atoms and present hydrogen bond interactions across the different layers. Hydroxyl groups located at the surface of MgO grains are likely to be involved in the gate-driven dehydration presented here. Under a negative gate voltage applied to the top electrode, oxygen species migrate into the stack, and could typically induce oxidation in the Co and Fe atoms.[3,4] In the present case, the migration of oxygen containing ions, most likely through the MgO grain boundaries, could rather be interacting with the H^+ ions from the hydroxyl groups at the surface of the MgO grains to form H_2O molecules and expand the volume of crystalline MgO.

A decrease in the OH ion content inside the stack after negative voltage gating is confirmed by the time of flight secondary ion mass spectrometry (ToF-SIMS) measurements presented in **Figure 5a–c**. Figure 5a shows the distribution of OH, Co, Fe and ^{30}Si ions. The highest contents of Co and Fe coincide at a sputtering time of about 82 s and are identified as the center of the CoFeB layer. Moving toward higher sputtering times, the signal decreases up to the point where the ^{30}Si signal increases, marking the vicinity of the Ta/SiO_2 interface. Similarly, by moving from the center of the CoFeB layer toward lower sputtering times an increase in the MgO and ^{18}O signals is evidenced, which indicates the vicinity of the CoFeB(Pt)/MgO interface. The shaded area between 80 s and 42 s indicates the approximate position of the MgO layer, the upper limit of 42 s is chosen based on the change of slope seen in the profiles of OH, MgO, and ^{18}O below 50 s. The ^{18}O and MgO profiles, shown in Figure 5b,c, respectively, are convoluted with the SiO_2 and SiC signals at high sputtering times due to mass interference, and do not evolve significantly after gating with negative voltages. Interestingly, the OH profile evolves independently of the ^{18}O and MgO profiles, showing a clear decrease in content in the region corresponding to the position of the MgO layer after gating with negative voltages as shown in Figure 5a. This further supports the idea of a gate induced loss of hydroxyl groups, which can be related with the dehydration of regions in the MgO layer that are rich in $Mg(OH)_2$. Furthermore, X-ray photoelectron spectroscopy measured in the binding energy range corresponding to the Mg 2s levels clearly shows a shift of the broad main peak of approximately 0.7 eV toward lower binding energies, while the Pt peaks remain unaffected. Studies in the literature show that a shift of the Mg 2s peak to lower binding energies can be evidence of a larger contribution of MgO with respect to $Mg(OH)_2$,[35] in agreement with the proposed scenario of an increase in the $MgO/Mg(OH)_2$ ratio after gating with negative voltages.

The proposed gate-induced dehydration of $Mg(OH)_2$ in favor of the formation of MgO is likely to reach a saturation point after a prolonged exposure to gating, given the finite amount of $Mg(OH)_2$ in the system. Therefore, the irreversible effects induced on magnetic anisotropy are also expected to progressively disappear for long gating times, to finally expose only the reversible effects. This scenario was evaluated by conducting a relatively long series of 300 gate voltage pulses, alternating between
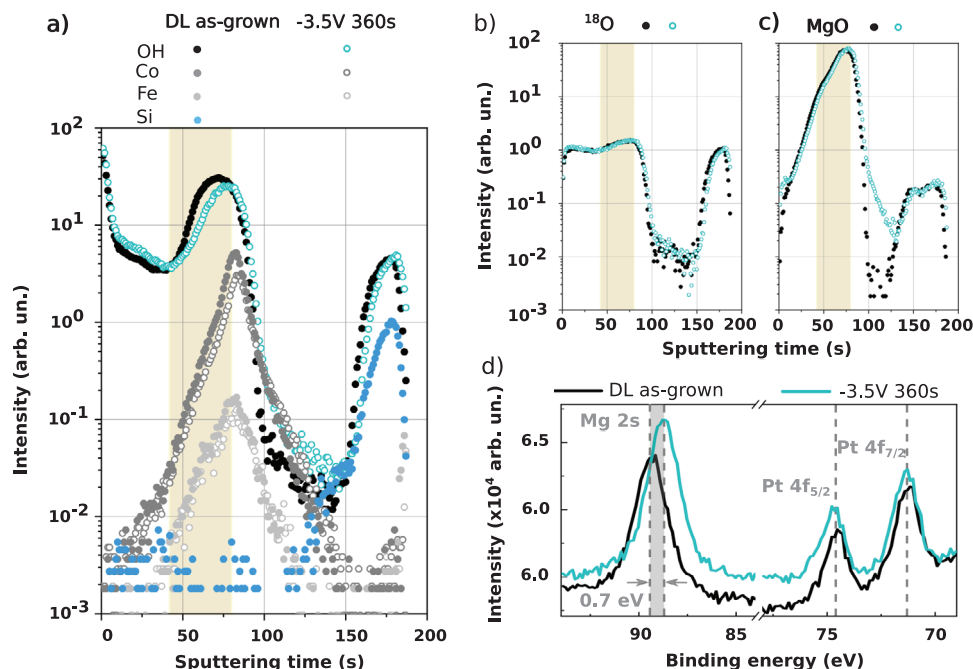
Figure 5. ToF-SIMS measurements before (filled black symbols) and after negative voltage gating (cyan open symbols) for OH (a), ^{18}O (b) and MgO (c). Co, Fe and Si are also shown in (a). The shaded area corresponds to the position of the MgO layer. XPS spectra before and after gating in the binding energy range of the Mg 2s levels and the Pt $4f_{5/2}$ and $4f_{7/2}$ levels.

negative and positive gate voltages. In this case, solid state gating devices were fabricated in order to evaluate the behavior of this complex system in a device geometry more compatible with spintronics applications and to rule out any potential contribution from the ionic liquid. Solid state gating allows also to compare the performance with respect to ionic liquid gating devices: while the solid state devices allow for faster operation (2s gate pulses), since they do not include the ion dynamics inside the ionic liquid, the gate voltages needed to induce similar changes as those induced by ionic liquid gating are significantly higher (+/−11V) due to the enhanced efficiency of the ionic liquid to produce high electric fields. **Figure 6** shows in Figure 6a an optical image and schematics of the solid-state gate devices fabricated from a DL-sample continuous film. In this device geometry, the ionic liquid is replaced by a 20 nm thick HfO_2 layer grown by atomic layer deposition. Using these devices, a series of 300 gate pulses was conducted, in which each pulse duration is 2s and the gate voltage alternates between −11 and +11 V. After each pulse, a hysteresis loop is recorded from which the total AHE amplitude and the AHE voltage at 0.5 mT have been extracted. Recording the AHE voltage at 0.5 mT allows to clearly follow the changes in magnetic anisotropy also in the dominant IPA regime, where the remanence in the z direction is negligible. Figure 6b shows the dependence of the total AHE amplitude (open symbols) and the AHE voltage at 0.5 mT (filled symbols) on the pulse number for gate voltages of −11 V (cyan) and +11 V (lime). Within the first 150 pulses, a large variation of the AHE voltage at 0.5 mT is observed, which can be directly linked to a rapid increase in the PMA component in the device. Although a large degree of reversibility is observed between positive and negative gate voltage pulses, the general trend of increase in the PMA component is visible not

only after negative gate voltages but also after positive gate voltages. Negative gate voltages bring the system to a PMA state that is relatively similar after about 30 pulses, while positive voltages are progressively leaving the system in states with a higher PMA component up to approximately 150 pulses, moving significantly away from the IPA state of the as-grown system for each gate voltage application. The top panel of Figure 6c shows hysteresis loops of the first application of negative gate voltage and of the pulses with numbers between 9 and 12, showing the evolution toward stronger PMA after negative gate voltage pulses and a damped return to an IPA dominated state for positive gate voltages. The magneto-ionic behavior within this gate pulse range closely resembles the one presented in Figure 1, which confirms the equivalence of the ionic-liquid and solid-state gating methods and the intrinsic nature of the magneto-ionic effects presented. This behavior clearly shows that a superposition of reversible and irreversible effects is at play. The middle panel in Figure 6c shows hysteresis loops between gate pulse numbers 56 and 59, which shows a full spin reorientation transition between a state with almost zero remanence and a robust PMA state with 100% remanence. In this range the non-reversible effects are imperceptible, and can only be seen by considering the general trend of the gate voltage series presented in Figure 6a. Finally, the gate voltage cycling seems to reach a steady regime, in which reversible effects are dominant for gate pulses number higher than 150. The inset in Figure 6a shows a zoomed-in view of this region, where a reversible effect between positive and negative voltages is seen to occur with only a minor drift present up to approximately 220 cycles. The bottom panel of Figure 6c shows gate voltage pulses between 268 and 271, within the steady state regime, where full reversibility is observed between two distinct states that are now
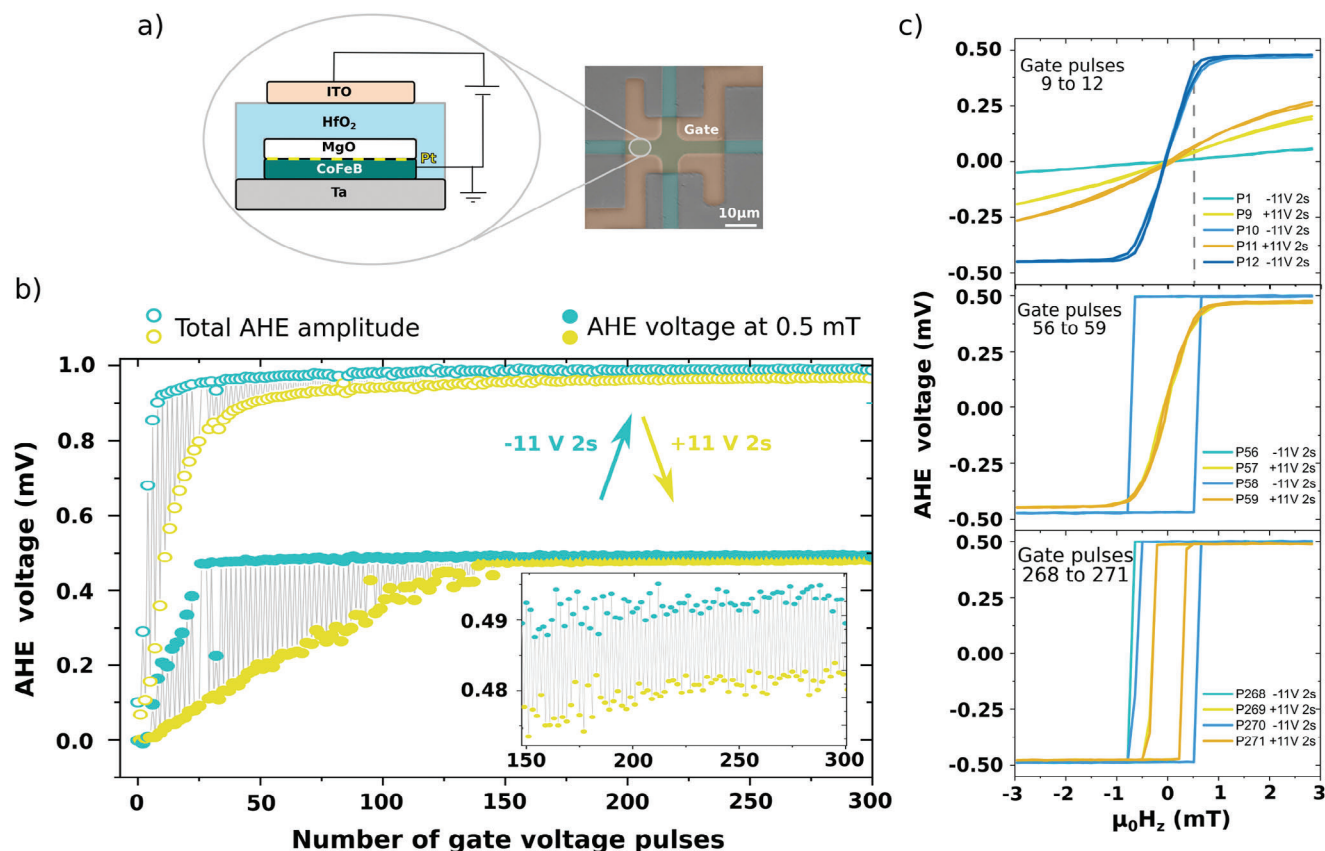
ADVANCED
SCIENCE NEWS

www.advancedsciencenews.com

ADVANCED
MATERIALS
INTERFACES
Open Access

www.advmatinterfaces.de

Figure 6. a) Optical image and schematics of a solid state gating device fabricated using DL samples. b) Total AHE amplitude (open symbols) and AHE voltage at 0.5 mT (full symbols) as a function of the number of applied gate voltage pulses. Voltage pulses alternate between -11 V (cyan) and +11 V (lime), each pulse is applied for 2 s. c) Hysteresis loops measured after gate voltage pulses between 1 and 12 (top), 56 to 59 (middle) and 268 to 271 (bottom). The vertical dotted line in the top panel in (c) indicates 0.5 mT.

within the PMA regime. Although the changes in the amplitude are minimal, as the two states have PMA, a significant change in the coercive field is induced by magneto-ionic gating which can certainly be exploited for reliable magneto-ionic functionalities in spintronics devices.

This measurement series shows that the gate induced changes in the crystalline structure of the MgO layer presented earlier translates into a progressive enhancement of the PMA component that saturates after sufficient gate voltage cycling. This enhancement can be understood as the progressive dehydration of the MgO, which could lead to the development of a higher contact surface between MgO and CoFeB, which in turn could favor PMA. This emphasizes the notion that changes in the structural order at the metal-oxide interface, even in the absence of oxidation, have the potential to induce significant modifications in magnetic anisotropy. The impact of magneto-ionic gating on crystalline structure is often overlooked, but as demonstrated here, it constitutes a critical factor in the emergence of irreversible effects in magneto-ionic devices. On the other hand, the reversible effects observed may be due to gentle non-oxidative interactions between Co and Fe and the oxygen atoms at the interface. The impact of oxygen content at the Fe/MgO interface on magnetic anisotropy has been investigated by first principles calculations[41] showing that both reversible and irreversible ef-

fects can be expected. The reversible effects are associated with small oxygen displacements and charge effects, while irreversible effects are ascribed to irreversible oxygen ion migration. Similar results have been obtained for a Fe/HfO$_2$ interface.[42] This supports the idea that a non-oxidative magneto-ionic mechanism, most likely involving small oxygen atom displacements at the CoFeB(Pt)/MgO, drives the reversible effects observed.

3. Conclusion

This study shows that magneto-ionic gating effects can be obtained in CoFeB/Pt/MgO/HfO$_2$ in the absence of oxidation of the Co and Fe atoms, which was investigated by XAS before and after ionic-liquid gating. The coexistence of reversible and irreversible magneto-ionic effects has been identified and probed by ionic-liquid and solid-state gating. Both reversible and irreversible effects on magnetic anisotropy can be observed in the first gating cycles in a series of gate voltage applications of alternating sign (below 150 gate pulses). Within this range, a gate-induced spin-reorientation transition can be observed on top of a general increase in the PMA component in the system. Beyond 150 gate pulses, the irreversible effects saturate and the reversible effects are dominant, where gate voltages can switch the anisotropy between two distinct states within the PMA

2300955 (8 of 10)

regime. We provide strong evidence that the irreversible oxygen-based magneto-ionic process is linked to dehydration in the MgO layer, increasing the ratio between MgO and $Mg(OH)_2$, which progressively strengthens the PMA component in the system over an extended gate pulse series, without preventing the reversible mechanisms from occurring. The reversible effects have been associated to potential gate-induced displacements of the oxygen atoms at the CoFeB(Pt)/MgO interface, modulating the interaction between oxygen and Fe/Co in a non-oxidative way. The results presented here are therefore important for oxygen-based magneto-ionics, since the gate-induced oxidation/reduction of the Co and Fe atoms has been so far discussed as the lead mechanism driving the gating effects in these systems. Moreover, the identification of reversible and irreversible effects brings light into the complex reversibility issues that can be encountered in magneto-ionic systems. Finally, the fact that a negative gate voltage can drive the dehydration of $Mg(OH)_2$ and produce an increase in the crystallinity of MgO, indicates that ionic gating can be used not only to provide dynamic magneto-ionic functionalities but can also be used as a powerful non-thermal and low-power method to control the crystallinity of MgO layers in both spintronics and memristive devices after fabrication.

4. Experimental Section

Sample Preparation and E-Field Gating: The magnetic stack used in this study was grown using a Singulus Rotaris deposition system equipped with magnetron targets. Metals (Ta, $Co_{40}Fe_{40}B_{20}$, Pt) were DC-sputtered and MgO and HfO_2 were RF-sputtered. Before the deposition of the film, a base pressure of 4×10^{-8} mbar was achieved. The deposition was performed at magnetron output powers 100, 400, and 950 W for Ta, $Co_{40}Fe_{40}B_{20}$, and HfO_2, respectively while keeping the gas flow of Ar (process gas).

The stacks were gated by adding ionic liquid (IL) $[EMI]^+[TFSI]^-$ (1-Ethyl-3-methylimidazolium bis (trifluoromethanesulfonyl)imide) to the surface of the film followed by placing a glass substrate coated with a 100 nm thick indium tin oxide (ITO) layer to apply the *E*-field. Experiments were performed at room temperature on samples cut from the same wafer and all magnetic states presented here were measured after the the gate-voltage was switched off and the liquid gate removed from the surface of the sample. The sole exception to the latter was anomalous Hall effect measurements, where the liquid gate was present in all measurements.

Solid state gating devices were fabricated using photo-lithography, ion beam etching, metal deposition, and lift-off. A layer of 20 nm of HfO_2 was grown on top of the as-grown DL stack by atomic layer deposition at 100 °C, the gate top electrode was made by sputtering 50 nm of ITO. The AHE voltages informed were obtained using a bias current of 200 µA.

XAS Measurements: XAS was performed at the DEIMOS beamline[43,44] at the Synchrotron SOLEIL using total electron yield (TEY). Spectra presented for DL gated measurements (as-grown, negative and positive gate voltages) were conducted on the same sample. First, the sample was measured in the as-grown state, then negative, and subsequently positive voltages were applied to the same sample. XAS experiments were conducted after each voltage application.

XRD Measurements: Grazing incidence X-ray diffraction measurements were performed at the SixS beamline at the Synchrotron SOLEIL at a wavelength of 0.673 Å. For ease of comparison with literature, the angles given here correspond to an energy of Cu K-alpha1 (1.54 Å). In-plane maps were recorded at a range of at least 180° rotation of the sample for different incidence angles. The XRD curve for +4 V 360 s belonged to the same DL sample which was used in XAS and the DL as-grown sample was a fresh sample cut from the same wafer. A fresh DL sample from the same wafer was prepared, and a voltage of −3.5 V was applied to it for 360 s.

X-Ray Photoelectron Spectroscopy (XPS): XPS was performed using a PHI ESCA 5600 (PHI Electronics) apparatus equipped with a monochromatic Al Kα X-ray source (1486.6 eV) and a hemispherical analyzer, with pass energy equal to 57.80 eV and energy resolution 0.125 eV.

Time of Flight Secondary Ion Mass Spectrometry (ToF-SIMS): ToF-SIMS depth profiles were collected in an upgraded ION-TOF IV instrument (ION-TOF GmbH) using 500 eV Cs+ ions for sputtering a 300 µm × 300 µm area and 25 keV Ga+ ions with an energy of 25 keV for the analysis of a 50 µm × 50 µm area at the center of the sputtered region, operating in interlaced mode. Secondary ions were collected in negative polarity and the collected intensities normalized to the signal of $^{18}O^-$ in the middle of the HfO_2 layer. ^{18}O was selected as a robust signal to probe Oxygen because its natural abundance (0.2%) allowed to avoid saturation in detection in oxide layers, such as HfO_2 and MgO, a situation occurring if ^{16}O, the most abundant Oxygen isotope, would be considered.

Supporting Information

Supporting Information is available from the Wiley Online Library or from the author.

Conflict of Interest

The authors declare no conflict of interest.

Data Availability Statement

The data that support the findings of this study are available from the corresponding author upon reasonable request.

[1] U. Bauer, L. Yao, A. J. Tan, P. Agrawal, S. Emori, H. L. Tuller, S. van Dijken, G. S. D. Beach, *Nature Mater.* **2015**, *14*, 174.

[2] U. Bauer, S. Emori, G. S. D. Beach, *Nature Nanotech.* **2013**, *8*, 411.

[3] L. Herrera Diez, Y. Liu, D. Gilbert, M. Belmeguenai, J. Vogel, S. Pizzini, E. Martinez, A. Lamperti, J. Mohammedi, A. Laborieux, Y. Roussigné, A. Grutter, E. Arenholtz, P. Quarterman, B. Maranville, S. Ono, M. S. E. Hadri, R. Tolley, E. Fullerton, L. Sanchez-Tejerina, A. Stashkevich, S. Chérif, A. Kent, D. Querlioz, J. Langer, B. Ocker, D. Ravelosona, *Phys. Rev. Appl.* **2019**, *12*, 034005.

[4] R. Pachat, D. Ourdani, M.-A. Syskaki, A. Lamperti, S. Roy, S. Chen, A. D. Pietro, L. Largeau, R. Juge, M. Massouras, C. Balan, J. W. van der Jagt, G. Agnus, Y. Roussigné, M. Gabor, S. M. Chérif, G. Durin, S. Ono, J. Langer, D. Querlioz, D. Ravelosona, M. Belmeguenai, L. Herrera Diez, *Adv. Mater. Interfaces* **2022**, *9*, 2200690.

[5] T. Bhatnagar-Schöffmann, A. Kovàcs, R. Pachat, D. Ourdani, A. Lamperti, M.-A. Syskaki, T. da Câmara Santa Clara Gomes, Y. Roussigné, S. Ono, J. Langer, M. Cherif, R. E. Dunin-Borkowski, P. Schöffmann, D. Ravelosona, M. Belmeguenai, A. Solignac, L. Herrera Diez, *Appl. Phys. Lett.* **2023**, *122*, 042402.

[6] T. Ueno, J. Sinha, N. Inami, Y. Takeichi, S. Mitani, K. Ono, M. Hayashi, *Sci. Rep.* **2015**, *5*, 14858.

[7] C. Martinez-Boubeta, L. Balcells, B. Martínez, *J. Appl. Phys.* **2013**, *113*, 123908.

[8] M. Giménez-Marqués, E. Bellido, T. Berthelot, T. Simón-Yarza, T. Hidalgo, R. Simón-Vázquez, Á. González-Fernández, J. Avila, M. C. Asensio, R. Gref, C. Serre, P. Horcajada, *Small* **2018**, *14*, 1801900.

[9] S. S. Lee, J. H. Kim, S. C. Wi, G. Kim, J.-S. Kang, Y. J. Shin, S. W. Han, K. H. Kim, H. J. Song, H. J. Shin, *J. Appl. Phys.* **2005**, *97*, 10A309.

[10] F. M. F. de Groot, M. Grioni, J. C. Fuggle, J. Ghijsen, G. A. Sawatzky, H. Petersen, *Phys. Rev. B* **1989**, *40*, 5715.

[11] F. Frati, M. O. J. Y. Hunault, F. M. F. De Groot, *Chem. Rev.* **2020**, *120*, 4056.

[12] Ph. Wernet, D. Nordlund, U. Bergmann, M. Cavalleri, M. Odelius, H. Ogasawara, L. Å. Näslund, T. K. Hirsch, L. Ojamäe, P. Glatzel, L. G. M. Pettersson, A. Nilsson, *Science* **2004**, *304*, 995.

[13] A. J. Tan, M. Huang, C. O. Avci, F. Büttner, M. Mann, W. Hu, C. Mazzoli, S. Wilkins, H. L. Tuller, G. S. D. Beach, *Nature Mater.* **2019**, *18*, 35.

[14] C. Y. Kim, K. S. Jeong, Y. S. Kang, S. W. Cho, M.-H. Cho, K. B. Chung, D.-H. Ko, Y. Yi, H. Kim, *J. Appl. Phys.* **2011**, *109*, 114112.

[15] D. H. Hill, R. A. Bartynski, N. V. Nguyen, A. C. Davydov, D. Chandler-Horowitz, M. M. Frank, *J. Appl. Phys.* **2008**, *103*, 093712.

[16] D. Telesca, B. Sinkovic, S.-H. Yang, S. S. P. Parkin, *J. Electron Spectrosc. Relat. Phenom.* **2012**, *185*, 133.

[17] D. Drevon, M. Görlin, P. Chernev, L. Xi, H. Dau, K. M. Lange, *Sci. Rep.* **2019**, *9*, 1532.

[18] M. Sinha, M. Gupta, P. Jonnard, M. H. Modi, *Surf. Interface Anal.* **2018**, *50*, 1145.

[19] D.-Y. Cho, C.-H. Min, J.-Y. Kim, J.-H. Park, S.-J. Oh, C. S. Hwang, *J. Phys.: Conf. Ser.* **2008**, *100*, 042044.

[20] L. Soriano, M. Abbate, J. C. Fuggle, M. A. Jiménez, J. M. Sanz, C. Mythen, H. A. Padmore, *Solid State Commun.* **1993**, *87*, 699.

[21] T. Mizoguchi, I. Tanaka, M. Yoshiya, F. Oba, K. Ogasawara, H. Adachi, *Phys. Rev. B* **2000**, *61*, 2180.

[22] L. Lin, P. Sherrell, Y. Liu, W. Lei, S. Zhang, H. Zhang, G. G. Wallace, J. Chen, *Adv. Energy Mater.* **2020**, *10*, 1903870.

[23] N. Cheng, S. Stambula, D. Wang, M. N. Banis, J. Liu, A. Riese, B. Xiao, R. Li, T.-K. Sham, L.-M. Liu, G. A. Botton, X. Sun, *Nat. Commun.* **2016**, *7*, 13638.

[24] H. Zhang, G. Liu, L. Shi, J. Ye, *Adv. Energy Mater.* **2018**, *8*, 1701343.

[25] B. Qiao, A. Wang, X. Yang, L. F. Allard, Z. Jiang, Y. Cui, J. Liu, J. Li, T. Zhang, *Nature Chem.* **2011**, *3*, 634.

[26] R. S. Alvim, I. J. Borges, D. G. Costa, A. A. Leitão, *J. Phys. Chem. C* **2012**, *116*, 738.

[27] E. Carrasco, M. A. Brown, M. Sterrer, H.-J. Freund, K. Kwapien, M. Sierka, J. Sauer, *J. Phys. Chem. C* **2010**, *114*, 18207.

[28] A. Kondo, R. Kurosawa, J. Ryu, M. Matsuoka, M. Takeuchi, *J. Phys. Chem. C* **2021**, *125*, 10937.

[29] L. Kumari, W. Z. Li, C. H. Vannoy, R. M. Leblanc, D. Z. Wang, *Ceram. Int.* **2009**, *35*, 3355.

[30] D. Su, N. Jiang, J. C. H. Spence, F. He, W. T. Petuskey, *J. Appl. Phys.* **2008**, *104*, 063514.

[31] T. Yoshida, T. Tanaka, H. Yoshida, T. Funabiki, S. Yoshida, T. Murata, *J. Phys. Chem.* **1995**, *99*, 10890.

[32] Y. S. Choi, Y. Nagamine, K. Tsunekawa, H. Maehara, D. D. Djayaprawira, S. Yuasa, K. Ando, *Appl. Phys. Lett.* **2007**, *90*, 012505.

[33] W. L. Peng, J. Y. Zhang, G. N. Feng, X. L. Xu, C. Yang, Y. L. Jia, G. H. Yu, *Appl. Phys. Lett.* **2019**, *115*, 092402.

[34] S. Sato, H. Honjo, S. Ikeda, H. Ohno, T. Endoh, M. Niwa, *Jpn. J. Appl. Phys.* **2016**, *55*, 04EE05.

[35] A. Le Febvrier, J. Jensen, P. Eklund, *J. Vac. Sci. Technol. A* **2017**, *35*, 021407.

[36] S. Iwasaki, S. Kodani, N. Koga, *J. Phys. Chem. C* **2020**, *124*, 2458.

[37] M. J. McKelvy, R. Sharma, A. V. G. Chizmeshya, R. W. Carpenter, K. Streib, *Chem. Mater.* **2001**, *13*, 921.

[38] E. Knözinger, K.-H. Jacob, S. Singh, P. Hofmann, *Surf. Sci.* **1993**, *290*, 388.

[39] C. Chizallet, G. Costentin, M. Che, F. Delbecq, P. Sautet, *J. Am. Chem. Soc.* **2007**, *129*, 6442.

[40] C. Chizallet, G. Costentin, M. Che, F. Delbecq, P. Sautet, *J. Phys. Chem. B* **2006**, *110*, 15878.

[41] F. Ibrahim, A. Hallal, B. Dieny, M. Chshiev, *Phys. Rev. B* **2018**, *98*, 214441.

[42] A. Di Pietro, R. Pachat, L. Qiao, L. Herrera-Diez, J. W. van der Jagt, S. Picozzi, D. Ravelosona, W. Ren, G. Durin, *Phys. Rev. B* **2023**, *107*, 174413.

[43] P. Ohresser, E. Otero, F. Choueikani, K. Chen, S. Stanescu, F. Deschamps, T. Moreno, F. Polack, B. Lagarde, J.-P. Daguerre, F. Marteau, F. Scheurer, L. Joly, J.-P. Kappler, B. Muller, O. Bunau, Ph. Sainctavit, *Rev. Sci. Instrum.* **2014**, *85*, 013106.

[44] L. Joly, E. Otero, F. Choueikani, F. Marteau, L. Chapuis, P. Ohresser, *J. Synchrotron. Rad.* **2014**, *21*, 502.